

**Linking radiomic PET features with metabolic tissue  
parameters using a hybrid mathematical model of tumor  
growth**

by

Hailey S.H. Ahn

A THESIS SUBMITTED IN PARTIAL FULFILLMENT  
OF THE REQUIREMENTS FOR THE DEGREE OF

**Bachelor of Science in Honours Biophysics**

in

THE FACULTY OF SCIENCE

(Physics and Astronomy)

The University of British Columbia

(Vancouver)

April 2021

© Hailey S.H. Ahn, 2021

# Abstract

Tumor heterogeneity can be observed between and within tumors through medical imaging such as positron emission tomography (PET). Heterogeneity arises due to the genetic diversity in cancer cell populations and the dynamic microenvironments. Understanding the relationship between tumor tissue microparameters and quantitative PET radiomic features can offer a better strategy for cancer diagnosis and treatment. Our goal was to develop a multiscale mathematical model for realistic tumor growth in vascularized tissue, and to generate synthetic PET images from the simulated images to study this relationship. The hybrid mathematical model used in the simulation combines an agent grid and partial differential equations to model the dynamic tumor microenvironments. The status of the cell and its behaviour is determined by the local concentration of oxygen and glucose which diffuse from the vessels to tissue. The simulated cell maps were converted to synthetic PET images by translating the spatial locations of the cells to the corresponding pseudo-standardized tracer uptake values of the PET tracer  $^{18}\text{F}$ -fluorodeoxyglucose, which are unique to each cell type. Using different combinations of tissue microparameters, we were able to generate tumors with distinct phenotypic profiles that were visually distinguishable in the translated synthetic PET images. Four radiomic features were computed from the resulting images and this demonstrated that unique tumor phenotypes can be linked to radiomic PET features. Moreover, the identified optimal radiomic features can be used as biomarkers for tumor assessment.

# Table of Contents

<b>Abstract . . . . .</b>	<b>ii</b>
<b>Table of Contents . . . . .</b>	<b>iii</b>
<b>List of Tables . . . . .</b>	<b>v</b>
<b>List of Figures . . . . .</b>	<b>vi</b>
<b>Acknowledgments . . . . .</b>	<b>x</b>
<b>1 Introduction and Motivation . . . . .</b>	<b>1</b>
<b>2 Theory and Background . . . . .</b>	<b>5</b>
2.1 Cancer Biology . . . . .	5
2.1.1 Normal and Tumor Cell Metabolism . . . . .	6
2.1.2 Tumor Vascular Network and Alterations . . . . .	8
2.1.3 Hypoxia . . . . .	8
2.1.4 Apoptosis and Necrosis . . . . .	9
2.2 Positron Emission Tomography . . . . .	11
2.2.1 Radiotracer . . . . .	11
2.2.2 Signal Detection and Reconstruction . . . . .	12
2.3 Radiomic Features . . . . .	14
2.3.1 Image Acquisition and Segmentation . . . . .	15
2.3.2 Radiomic Features Extraction . . . . .	15
2.3.3 Features Analysis . . . . .	19

2.4	Hybrid Mathematical Modeling . . . . .	20
2.4.1	Agent Grid . . . . .	20
2.4.2	Partial Differential Equation Grid . . . . .	20
<b>3</b>	<b>Methods . . . . .</b>	<b>23</b>
3.1	Tumor Growth Model . . . . .	23
3.1.1	Types of Agents . . . . .	23
3.1.2	Simulation Details . . . . .	24
3.2	Translating Simulated Images to PET Images . . . . .	25
3.2.1	Advantages of Using Synthetic PET Images . . . . .	27
3.3	Radiomics Analysis . . . . .	28
<b>4</b>	<b>Results . . . . .</b>	<b>29</b>
4.1	Agent Grid + Oxygen PDE Grid . . . . .	29
4.2	Agent Grid + Oxygen and Glucose PDE Grids . . . . .	30
<b>5</b>	<b>Discussion . . . . .</b>	<b>35</b>
<b>6</b>	<b>Future Directions . . . . .</b>	<b>38</b>
	<b>Bibliography . . . . .</b>	<b>40</b>

# List of Tables

Table 2.1	Semantic and agnostic radiomic features . . . . .	19
Table 3.1	Model biological parameters . . . . .	24
Table 3.2	MATLAB functions for radiomics analysis. . . . .	28
Table 4.1	Radiomic feature values for 1cm tumors. . . . .	31

# List of Figures

Figure 1.1	<b>PET/CT image of a pancreatic cancer patient.</b> Demonstration of how the CT scan (A) and a PET scan (B) is integrated to provide a high resolution functional and anatomical image (C). The merged image allows localization of the FDG uptake values in the PET scan. Figures adapted from [5]. . . . .	2
Figure 1.2	<b>Identification and validation of radiomic biomarkers for precision medicine.</b> There are two ways of developing imaging biomarkers: extraction of hand-crafted features and data-driven deep learning models. The identified features an be used for patient-specific decision making and prediction of clinical outcomes. Figure from [19] . . . . .	4
Figure 2.1	<b>Tumor and normal cell metabolism.</b> The three cellular metabolic pathways are illustrated. Tumor cells exhibit modified metabolism that utilizes the aerobic glycolysis pathway, which is called the Warburg effect. Figure from [35] . . . . .	7
Figure 2.2	<b>Aerobic, hypoxic, and necrotic regions with distance from the blood vessel.</b> Cells that are in close proximity of the vessel are viable aerobic cells. However, with increasing distance from the vessel hypoxic and necrotic cells arise. Figure from [3].	9
Figure 2.3	<b>Survival curve of normal tumor and hypoxic tumor cells.</b> Hypoxic cells exhibit reduced radiation sensitivity and requires a much higher radiation dose to achieve the equivalent effectiveness as in oxic cells. Figure from [27] . . . . .	10

Figure 2.4	<b>Radioisotope decay and annihilation event.</b> The radioactive atom attached to the radioisotope goes through a beta decay and produces a positron ( $\beta^+$ ). The positron travels a few millimeters until it loses most of its kinetic energy and annihilates with a nearby electron ( $\beta^-$ ). The annihilation event produces a pair of 511keV photons in opposite directions. If the two photons are observed by the scintillation detectors within the coincidence time window, the annihilation event is recorded. Figure from [29] . . . . .	12
Figure 2.5	<b>Positron emission tomography signal detection and image construction.</b> (a) The red circle represents one pixel of the PET image where coincident events are recorded by the detectors along the lines of response (LORs). The angle and displacement of the LORs are measured with respect to the red horizontal line and the center of field of view. (b) A sinogram where the four LORs from panel (a) are added up over the scanning period. For example, LOR4 is along the center, so the displacement is 0 and it makes a right angle with the horizontal line, so the angle is $90^\circ$ . The total counts along the four LORs are stored in each position of the sinogram. (c) A sinogram of all pixels in the image plane and darker spots indicate greater number of counts. Figure from [29] . . . . .	14
Figure 2.6	<b>Radiomics analysis pipeline.</b> (a) Image acquisition via computed tomography. (b) Image segmentation is performed on the lesion to identify the ROI. (c) Radiomic features are extracted from the ROI. The three feature categories are gray level patterns, inter-voxel relationships, and shape. (d) Analysis and classification of a subset of selected features. (e) Selected features are used as biomarkers in diagnosis and patient prognosis. Figure from [30] . . . . .	16

Figure 2.7	<b>Gray level co-occurrence matrix computation.</b> (a) Shows how adjacency is defined given a pixel of interest (red). The four possible angles are labeled and any choice of distance can be used to compute the GLCM. (b) An example of how an image matrix is translated to a GLCM matrix. The parameters used are $D=1$ and $\theta = 0^\circ$ . Figure adapted from [25] and [4]. .	18
Figure 2.8	<b>Hybrid mathematical modelling with agent and PDE grids.</b> The illustration shows one agent grid holding an agent (yellow dot) and two PDEs for oxygen and glucose. All grids can interface easily and the agent can retrieve the information from the corresponding pixels in the PDEs (yellow border). . . . .	21
Figure 3.1	<b>Tumor growth simulation flowchart.</b> The flowchart shows the step sequence of how the simulation is initialized, how agents determine their state, and how the PDE grids function (diffusion and consumption of molecules) . . . . .	26
Figure 3.2	<b>Moore neighbourhood.</b> Represents the eight locations surrounding the center pixel, in this case an agent, that border an edge or a corner of the cell. The arrows indicate the possible locations an agent can divide into in a Moore neighbourhood. Figure adapted from [9] . . . . .	27
Figure 4.1	<b>Simulated tumors with distinct tumor phenotypes.</b> The model with different combinations of tumor tissue microenvironments was able to produce three tumor types with distinct tumor phenotypes. . . . .	30
Figure 4.2	<b>Translation of the Type C tumor longitudinal growth simulation to PET images.</b> Simulated images were translated into synthetic PET images by converting the cell map into corresponding pSUV values. . . . .	31
Figure 4.3	<b>Biological time for tumor growth.</b> The cell count was plotted against the biological time to compare the growth rate of each tumor type. The tumors were grown up to $\sim 1cm$ in diameter.	32



Figure 4.4	<b>Radiomics analysis on synthetic PET images.</b> Four PET radiomic features were plotted against simulated biological time for tumor growth. The mean and standard deviations of the data points were calculated using three separate tumor growth simulation rounds. The error bar represents one standard deviation. . . . .	33
Figure 4.5	<b>Two distinct tumor phenotypes simulated with oxygen and glucose PDE grids.</b> The tumor progression is shown at three different time points (biological hours) until it reached 1cm in diameter. The bottom panels represent the magnifications of the regions indicated with the white box. . . . .	34

# Acknowledgments

I would like to express my sincere gratitude towards my supervisors Dr. Ivan Klyuzhin and Dr. Arman Rahmim from the Quantitative Radiomolecular Imaging & Therapy (QURIT) Lab at the BC Cancer Research Institute for the opportunity to work on this project. Their support and advice were what made this project possible and engaging despite of the remote nature of the work. I am also immensely grateful for my parents and my brother for their wholehearted support throughout my undergraduate degree. Many thanks to my dear friends as well, for shaping me the way I am today.

# Chapter 1

## Introduction and Motivation

Cancer refers to a class of diseases characterized by cells that proliferate at uncontrolled rates and spread throughout the body resulting in destruction of normal tissue. In fact, cancer accounted for about 9.6 million deaths in 2018, making it the second leading cause of death globally [7]. Benign tumors turn into malignant tumors as they acquire hallmarks for cancer progression, which includes resistance to programmed cell death (apoptosis), invasion of adjacent tissue, and induction of new blood vessel growth (angiogenesis). These hallmarks along with the dynamic tumor tissue microenvironments contribute to various phenotypes that introduce complications for cancer treatment.

Early detection and treatment for cancer have shown to effectively prevent progression of tumor which is crucial for patient survival. The most widely used method for cancer diagnosis is medical imaging and there are various modalities that allow physicians to detect abnormal properties of cancerous tissue such as increased metabolic activity or appearance without a surgical incision. The imaging methods are classified into three different categories: anatomic, functional, and molecular imaging. The typical resolution for medical images varies between each mode: 1mm for MRI and CT; 2-5mm for PET. Oftentimes anatomical and functional imaging methods are used together to acquire certain information that cannot be obtained via one imaging modality.

- **Anatomical Imaging** provides detailed structural information about the anatomy that yields high resolution clinical images. Magnetic resonance imaging

(MRI) and computed tomography (CT) imaging are examples of anatomical imaging modalities.

- **Functional Imaging** highlights physiological information including metabolism and local chemical composition. These imaging modalities include positron emission tomography (PET) and single photon emission computed tomography (SPECT) which provide information on tumor biological functions and microenvironment at a limited spatial resolution. Oftentimes, functional and anatomical images are used side by side for an integrated visualization of tumor biology with high resolution imaging (Figure 1.1).
- **Molecular Imaging** is used to obtain detailed pictures of human body at a molecular/cellular level. It provides functional information without the needs for more invasive procedures such as biopsy or surgery.

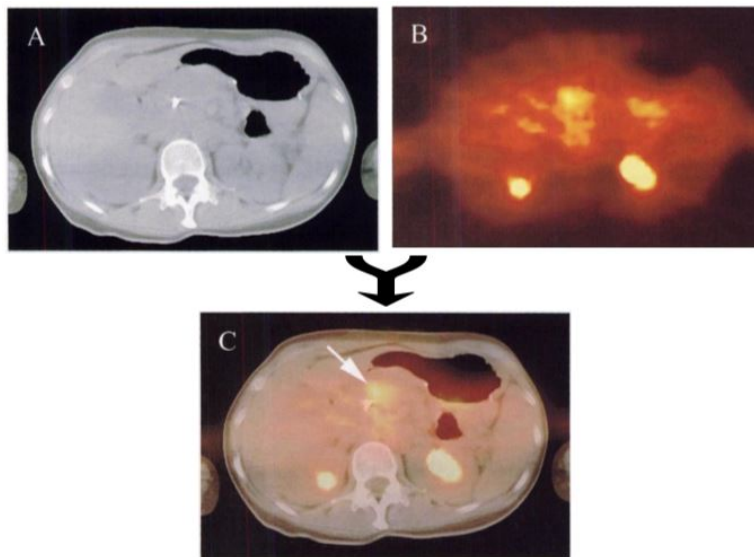


**Figure 1.1: PET/CT image of a pancreatic cancer patient.** Demonstration of how the CT scan (A) and a PET scan (B) is integrated to provide a high resolution functional and anatomical image (C). The merged image allows localization of the FDG uptake values in the PET scan. Figures adapted from [5].

There are four conventional types of cancer treatment: chemotherapy, radiation therapy, immunotherapy, and surgical removal of tumors. Surgical removal is only applicable when the tumor is accessible and has not metastasized. However, metastasis is prevalent in most cancers and requires other treatments involving high dose radiation that also kills healthy cells. The current strategy applied to cancer treatment is "one-size-fits-all", meaning that it has been standardized to be applicable to most people. However, this treatment approach is only effective in a subset of people due to the complexity in tumor intrinsic properties and progressions patterns that should be targeted differently [23]. In fact, a study performed in 2017 estimated that any particular category of standardized cancer drugs is ineffective in 75% of the patients [1]. The inherent variability in cancer led to the growing field of precision medicine which includes cancer genomics studies and radiomics analysis on medical images. Careful extraction and selection of meaningful information from these patient-specific approaches enable healthcare professionals to deliver customized treatment for increased efficiency and survival rates.

One of the emerging fields of precision medicine is radiomics, which is a method of converting medical images into high dimensional data with numerous quantifiable features. Analysis of these features can elucidate the underlying pathophysiology captured by medical images, revealing tumor characteristics that can assist cancer diagnosis, prognosis, and the development prediction models. Quantitative features based on size, shape, texture, and intensity can provide unique information about tumor heterogeneity and its microenvironments that cannot be obtained through other laboratory techniques [15]. There are hundreds of metrics that have been extracted from the images with the potential to reveal tumor characteristics that cannot be identified with human eyes [2]. The features can be carefully selected and used as biomarkers for patient-specific treatment planning and prognosis (Figure 1.2).

Tumor heterogeneity refers to observable variations in tumor phenotype and it can be observed through medical imaging or histopathological studies. Examples of heterogeneity are distinct morphologies, gene expression patterns, and sensitivity to treatment. Many research have shown that more heterogeneous tumors tend to exhibit more aggressive growth and resilience to treatment, leading to poor patient outcomes [18]. Additionally, tumors with similar characteristics have shown

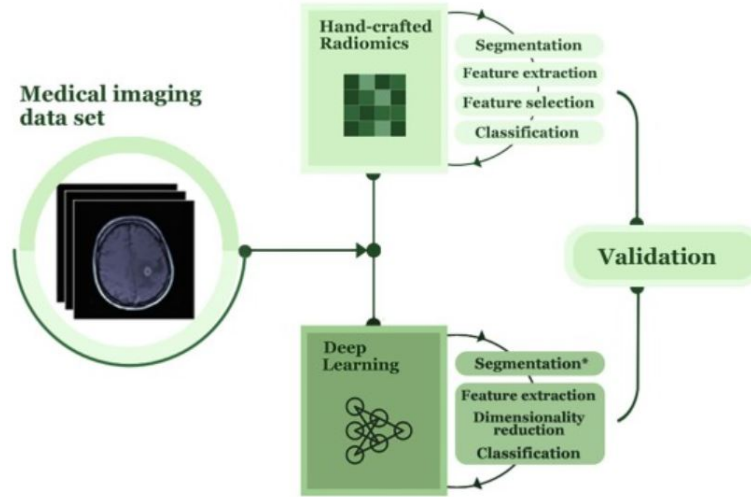


**Figure 1.2: Identification and validation of radiomic biomarkers for precision medicine.** There are two ways of developing imaging biomarkers: extraction of hand-crafted features and data-driven deep learning models. The identified features can be used for patient-specific decision making and prediction of clinical outcomes. Figure from [19]

similar progression patterns regardless of the location of the tumor [14, 17, 28]. Thus, understanding how tumor tissue microparameters are linked to observable features in medical imaging is of great interest. Unfortunately, we currently don't have a clear understanding of how specific tumor phenotypes are reflected in clinical images. Thus, our goal is to develop a multiscale mathematical model of realistic tumor growth in vascularized tissue, and use the simulated images to produce synthetic PET images showing metabolic profiles of the tumor. Performing radiomics analysis on these synthetic PET images allows us to establish a link between specific tumor phenotypes and tissue microparameters. More accurate and detailed characterization of the tumors using this approach enables optimized treatment based on individual tumor characteristics.

## Chapter 2

# Theory and Background

### 2.1 Cancer Biology

Cancer cells proliferate in uncontrolled manners, unlike normal cells with sophisticated balance between proliferation and differentiation until programmed cell death. Advances in cancer research revealed that cancer cells have mutations in their cell genome that disrupt this balance resulting in uncontrolled growth. When cancer is diagnosed in a patient, it has typically developed into solid tumor, which is a collection of many components such as cancer cells, healthy cells, blood vessels, and fibroblasts. The current speculation of a solid tumor is that it originates from a single tumor cell that has accumulated genetic mutations [10]. This cell proliferates forming a benign lesion, which progressively develops into malignant tumors with interactions with environmental factors such as carcinogens. A malignant tumor is capable of growing into normal tissue until it breaks through the basal membrane, which causes the cancer cells to spread to distant locations via a process called metastasis [39].

Despite of the uncontrolled proliferation patterns of tumor cells, their behaviour is dependent on the interactions with the tumor tissue microenvironments. It relies on external factors like signals from surrounding cells and the nutrient availability. This motivates the evaluation of solid tumors and their surrounding microenvironment as a whole, which allows us to observe the phenotypic variations in complex tumor tissue. Progression of solid tumors leads to drastic changes in the tumor

environment; for example, growing tumors can alter vascular networks by enhancing or inactivating vessels, invade into normal tissue, and become resistant to the host's immune response. The interactions between genetic diversity in tumor cells and modified tumor microenvironments give rise to both intra- and intertumoral heterogeneity. Previous studies have shown that tumors with similar phenotypic profiles show similar progression patterns and patient outcomes even if the tumors are located in different parts of the body [14, 17, 28]. There is also evidence that supports the claim that more heterogeneous tumors are often more aggressive and resistant to cancer treatments [18]. Hence, understanding how tumor heterogeneity is related to tumor prognosis and image properties is crucial for patient diagnosis and treatment planning. The following sections will explain the causes and mechanism of how heterogeneity arise in solid tumors.

### **2.1.1 Normal and Tumor Cell Metabolism**

Tumor cells proliferate at a much higher rate in comparison to normal cells due to mutations in the genes that regulate normal regulation of cell division. Because a cell division requires a lot of energy for biosynthesis of various proteins, cancer cells typically consume glucose and oxygen at a much higher rate relative to normal cells. Blood is the source of oxygen and glucose which diffuses through the tissue for cells to consume. Nutrient rich blood travels from the heart to different parts of the body through bulk motion and diffusion happens mostly at the capillary level. Capillaries are the ideal place for nutrients to diffuse out as the walls are made up of only a single layer of cells and the increased surface area with a typical diameter of  $\sim 5 - 12\mu m$  facilitates the diffusion process [36].

To understand cancer cell metabolism and how the different nutrient consumption rates arise, one needs to know the different metabolic pathways that cells take to generate adenosine triphosphate (ATP). The three pathways are oxidative phosphorylation (OXPHOS), anaerobic glycolysis, and aerobic glycolysis (Figure 2.1). A normal cell under oxygen saturated condition mainly utilizes the most efficient OXPHOS pathway for cellular metabolism, yielding 36ATP/glucose. Tumor cells, however, have shown to take the aerobic glycolysis pathway regardless of the presence of oxygen in the microenvironment, which only yields 4ATP/glucose; this is



only about one-ninth of what can be harvested through OXPHOS [35]. One of the most common speculation for this phenomenon is that glycolysis is up to  $\sim 100$  folds faster than that of OXPHOS, allowing cancer cells to produce much more ATP in a given time [20, 24]. However, this comes at a cost of increased glucose consumption due to the low efficiency of this metabolic pathway. This is called the Warburg Effect and it leads to the variations in glucose uptake rates that are most conveniently observed through PET imaging.

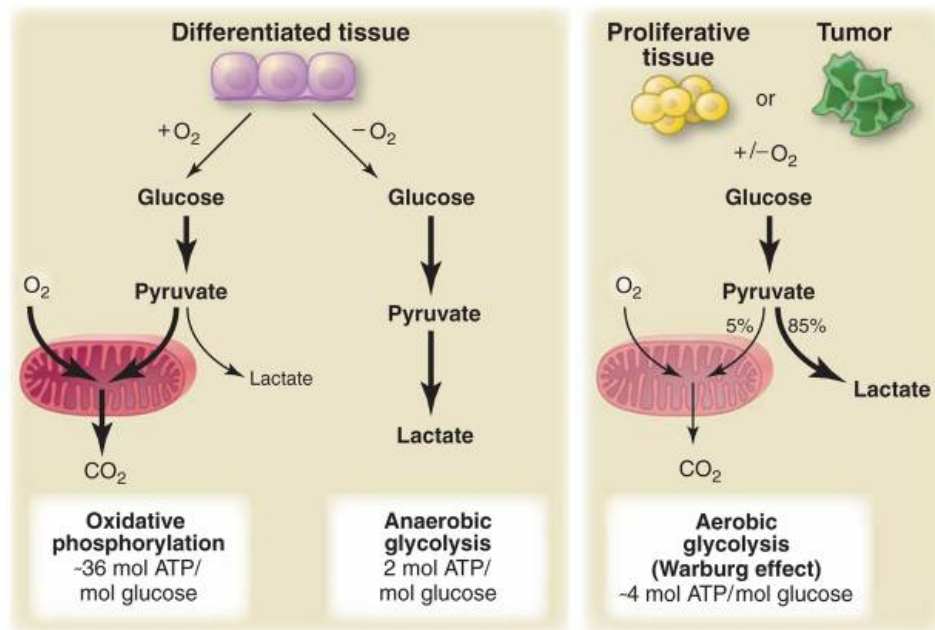


**Figure 2.1: Tumor and normal cell metabolism.** The three cellular metabolic pathways are illustrated. Tumor cells exhibit modified metabolism that utilizes the aerobic glycolysis pathway, which is called the Warburg effect. Figure from [35]

If a cell were to go through both OXPHOS and aerobic glycolysis, the combined net chemical equation for aerobic respiration becomes



with glucose (G), oxygen (O<sub>2</sub>), adenosine diphosphate (ADP), and phosphate (P)

[31].

### 2.1.2 Tumor Vascular Network and Alterations

The capillary network in the human body widely varies between tissue types. For instance, the skin has a capillary density of  $\sim 20/\text{mm}^2$  [33] and the skeletal muscle has  $\sim 100 - 500/\text{mm}^2$  [26]. Since tumor metabolism and rapid proliferation are closely associated with the supply of nutrients from the capillaries, where the tumor is located significantly influences the tumor progression patterns and the exhibited phenotype. The available oxygen and nutrients decrease with distance from the capillary. Hypoxia typically occurs at about  $100\mu\text{m}$  from the vessel and necrosis occurs at  $150\mu\text{m}$  (Figure 2.2) [3]. Moreover, tumor progression results in a number of vascular network alterations that give rise to observable heterogeneity in tumor tissue. This includes angiogenesis and dilated capillaries up to  $200\mu\text{m}$  in diameter [11]. On the other hand, with the rapid growth of solid tumors, host vessels are remodeled and pushed away, or even obstructed. Prolonged vessel occlusion causes necrosis to occur, typically starting at the center of the tumor that spreads outwards as more active vessels are removed by increasing cancer cell density [38]. Smaller vessels are first to be closed, followed by occlusion of larger vessels in later stages which leads to complete necrosis of the tumor.

### 2.1.3 Hypoxia

Hypoxia is one of the major contributors to tumor heterogeneity. It refers to a condition where a cell is deprived of oxygen supply due to increased oxygen consumption, inadequate oxygen diffusion from nearby blood vessels, or a combination of both. This phenomenon arises in solid tumors either in a diffusion-dependent (chronic) manner or as acute hypoxia if the vessel in the local environment becomes temporarily inactive. Thus, hypoxia itself is also a spatial and temporal heterogeneity and the dynamics are specific to the local neighborhood. It is also known to induce adaptive processes such as angiogenesis, which is a process where tumor tissue grows its own blood vessels to draw extra nutrients required for rapid proliferation. Moreover, hypoxia reduces the effectiveness of the treatment by reduction of the oxygen effect. The current treatment for cancer is to target cancer

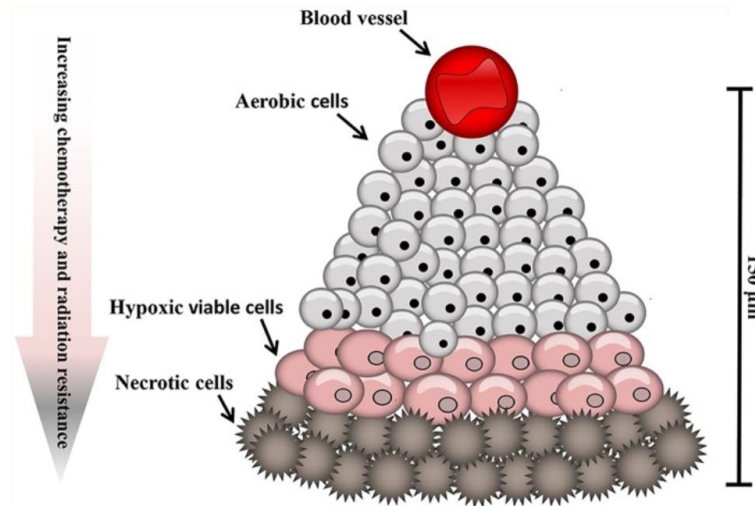


**Figure 2.2: Aerobic, hypoxic, and necrotic regions with distance from the blood vessel.** Cells that are in close proximity of the vessel are viable aerobic cells. However, with increasing distance from the vessel hypoxic and necrotic cells arise. Figure from [3].

cell DNA with high-energy radiation to cause damage and induce cell death. Here, oxygen acts as a radiosensitizer in radiotherapy by participating in chemical reactions that induce DNA damage. In fact, the direct effect of radiation to eliminate cancer cells only accounts for about 35%, and the other 65% is due to the oxygen effect [27]. Thus, hypoxic tumors require 2-3 times higher radiation dose relative to what oxygenated tumor tissue would require to be effective (Figure 2.3) [32].

#### 2.1.4 Apoptosis and Necrosis

There are two mechanisms for cell death, which are apoptosis and necrosis. Apoptosis refers to programmed cell death where cells that are damaged beyond repair commit to death at a certain point during their cell cycle. Cellular stimuli such as depletion of growth factors and hormones can also induce apoptosis. Apoptosis is a delicate ATP dependent process which any amount of disruption in its regulation can lead to devastating conditions like altered immune system functions and cancer. During the cell cycle, there are multiple checkpoints that ensure the cell is viable and is able to go through another round of division. A cell cycle arrest

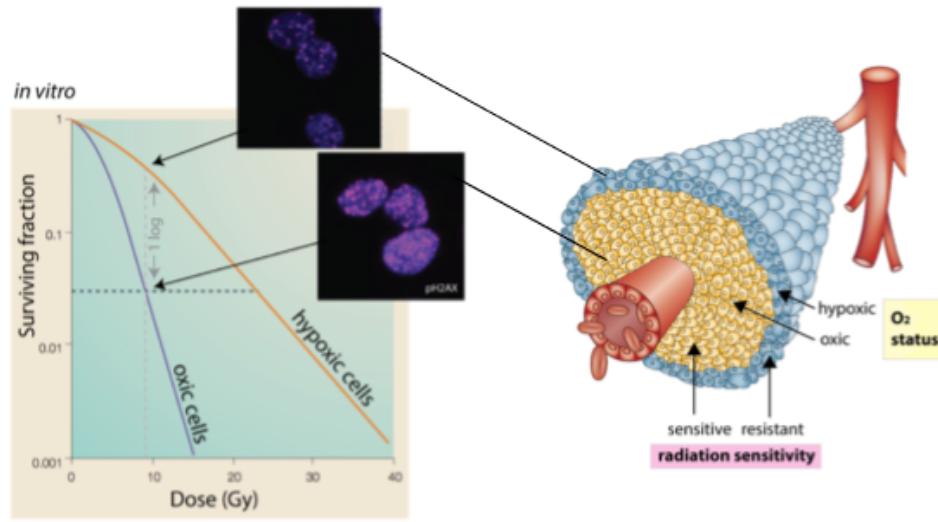


**Figure 2.3: Survival curve of normal tumor and hypoxic tumor cells.** Hypoxic cells exhibit reduced radiation sensitivity and requires a much higher radiation dose to achieve the equivalent effectiveness as in oxic cells. Figure from [27]

at one of the checkpoint initiates apoptosis which involves condensing of chromatin and organelles [12]. These collapsed cells are engulfed by macrophages in the body that digest the apoptotic cell and remove the waste products. The second form of cell death is necrosis. Unlike apoptosis, necrosis is caused by external stress, such as nutrient deficiency, and the process is independent of ATP availability. In general, there are two modes that trigger necrosis: cell death due to extreme hypoxia or ATP production below a threshold level. Because apoptosis involves multiple ATP-dependent steps, necrosis is the predominant pathway for cell death in a condition lacking ATP [12, 34]. A lump of necrotic cells called necrotic core is a phenomena frequently observed in solid tumors. This is caused by the rapid growth of solid tumors which makes it increasingly difficult for sufficient amount of nutrients to reach its core. Necrosis is not programmed like apoptosis and the process is triggered when one of the two conditions mentioned earlier is sustained for a prolonged period of time, ranging from hours to days [12]. Along with hypoxia, necrosis is one of the solid tumor characteristics that we modelled through

the tumor growth simulation.

## 2.2 Positron Emission Tomography

This section will go over the underlying physics of positron emission tomography, a medical imaging method that falls under the functional imaging category. Most of the information comes from *The Oxford Handbook of Functional Brain Imaging in Neuropsychology and Cognitive Neurosciences - Positron Emission Tomography: Blood Flow and Metabolic Imaging* [29] and *Nuclear Medicine Physics: The Basics* [8].

### 2.2.1 Radiotracer

Radiotracer refers to a molecule that is used up by organs during normal physiological processes with an additional radioactive atom attached. A small amount of this radioactive substance is injected into a patient's body to examine the metabolic activity of specific organs and tissue. A commonly used radiotracer for PET imaging is 18F-fluorodeoxyglucose (18F-FDG) which is an analog of 2-deoxy-D-glucose that is taken up by cells for metabolism. The attached radionuclide is fluorine-18 which undergoes  $\beta^+$ , emitting a positron. Although fluorine is not a physiologically relevant molecule, it is powerful for PET imaging purposes due to its half-life of  $\sim 2$  hours and the ease of substituting the hydroxyl group on glucose molecules without disturbing its biological properties. The positron emitted from the transient radioactive decay travels for a few millimeters and annihilates with an electron in the tissue, resulting in two photons that are emitted in opposite directions (Figure 2.4).

Cell proliferation costs large amounts of energy as it requires increased synthesis of macromolecules for a successful cell division. The increased energy demand and consequently increased glucose consumption leads to higher 18F-FDG uptake in tumors. A PET scan captures the change in metabolism, revealing spatial and temporal information of the tumor tissue.

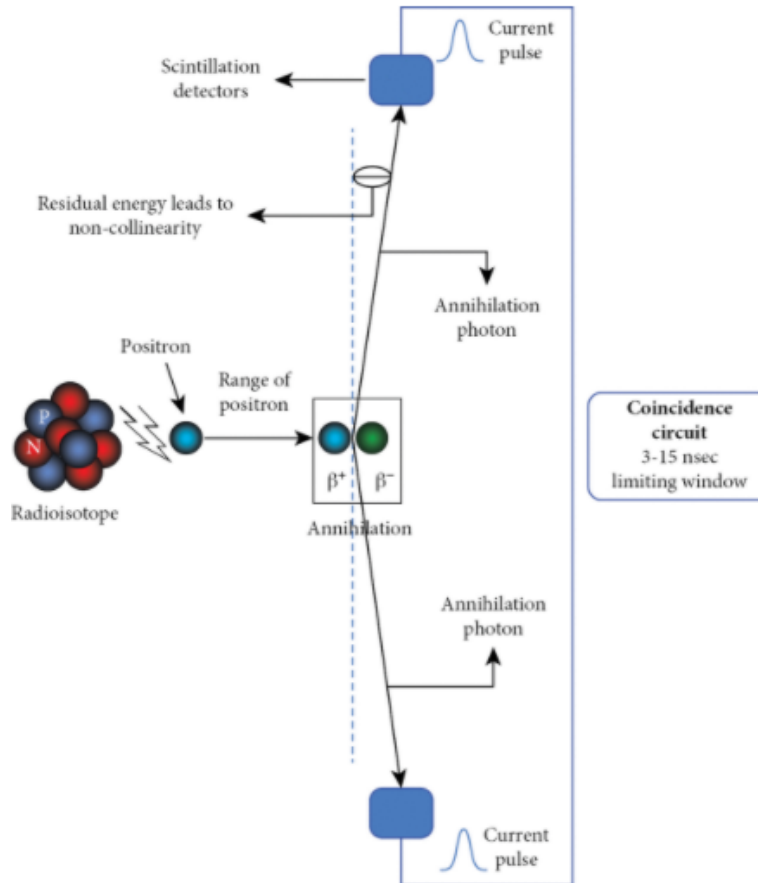


**Figure 2.4: Radioisotope decay and annihilation event.** The radioactive atom attached to the radioisotope goes through a beta decay and produces a positron ( $\beta^+$ ). The positron travels a few millimeters until it loses most of its kinetic energy and annihilates with a nearby electron ( $\beta^-$ ). The annihilation event produces a pair of 511 keV photons in opposite directions. If the two photons are observed by the scintillation detectors within the coincidence time window, the annihilation event is recorded. Figure from [29]

### 2.2.2 Signal Detection and Reconstruction

An illustration of a PET scanner with a patient situated inside the ring of photon detectors is shown in Figure 2.5. Soon after a small amount of radiotracer is injected

into the patient's body, the unstable proton inside the nucleus of a radioisotope goes through a  $\beta^+$  decay, releasing a positron. It travels for a few millimeters until it loses most of its kinetic energy and annihilates with an electron in tissue. The annihilation event produces two 511keV photons traveling in opposite directions. When these two gamma photons are detected by the PET scanner within a 6-12ns window, they are recorded as coincident events and the line of response (LOR) is defined. The LOR passes through the point of annihilation which eliminates the need for collimators, which is required in other imaging methods like single-photon emission computed tomography (SPECT) to prevent exposure from outside of the region of interest.

Inside each gamma camera, there are scintillators containing crystals ( $Lu_2SiO_5$  :  $Ce$  or  $Bi_4Ge_3O_{12}$ ) that allows radiation detection. These crystals produce light when high energy radiation is absorbed which is used to count the photons. Unless the pair of photons is emitted from the midpoint of the LOR, there exists a time delay between the detection of the two coincident photons. This is referred to as time of light (TOF) and it enables localization of the annihilation event. The signals are collected in the form of a sinogram (Figure 2.5 b,c) that needs to be corrected for sources of errors such as random coincidence events, scatter, and attenuation for a more accurate image reconstruction. The processed signal can be reconstructed through iterative or analytical methods.

In PET imaging, the radiotracer uptake is assessed through a semi-quantitative metric called standard uptake value (SUV). SUV is given by the equation:

$$SUV = \frac{\text{Tracer activity in tissue}}{\text{Total injected dose per patient weight}}.$$

The minimum, maximum, and mean SUV values can be computed from the region of interest based on the individual values stored in each pixel of the image. The computed values are used to assess the abnormal characteristics of tumor tissue, where malignant tumors typically have SUV values over 2.5-3 [21].

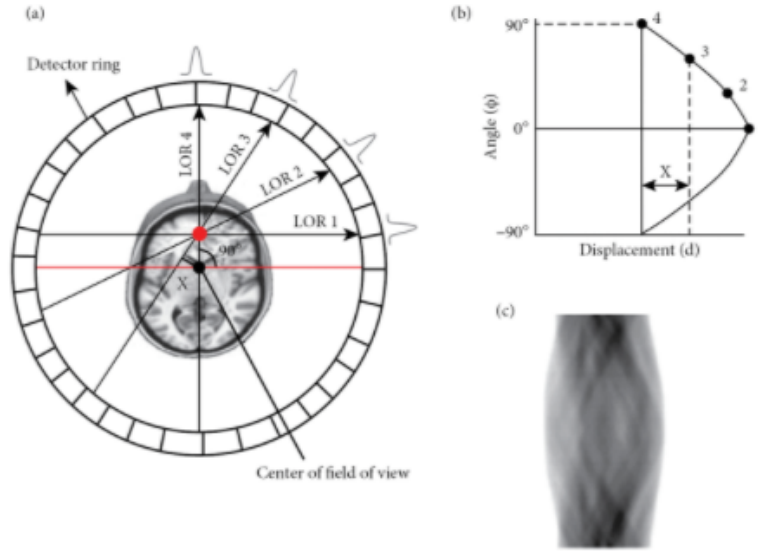


**Figure 2.5: Positron emission tomography signal detection and image construction.** (a) The red circle represents one pixel of the PET image where coincident events are recorded by the detectors along the lines of response (LORs). The angle and displacement of the LORs are measured with respect to the red horizontal line and the center of field of view. (b) A sinogram where the four LORs from panel (a) are added up over the scanning period. For example, LOR4 is along the center, so the displacement is 0 and it makes a right angle with the horizontal line, so the angle is  $90^\circ$ . The total counts along the four LORs are stored in each position of the sinogram. (c) A sinogram of all pixels in the image plane and darker spots indicate greater number of counts. Figure from [29]

## 2.3 Radiomic Features

Radiomics is a powerful tool used to extract quantitative information from clinical images. Radiomics analysis converts digital images to minable data, offering insight into the relationship between image properties and cancer phenotypic profiles. Due to the significant potential for elucidating unique tumor characteristics, it is an emerging field of research in medical physics with a main focus on developing novel biomarkers for cancer diagnosis and prognosis. The development of machine-learning models and processes for high-throughput extraction of im-



age features pushed the studies in the direction of developing prediction models rather than finding biological meaning from the analysis. There have been efforts to reconnect the prediction models and the biological significance through different approaches such as genomics and microscopic image texture (histological) studies. The four key steps of radiomics analysis are image acquisition, segmentation, quantitative image features extraction, and analysis of the features as shown in Figure 2.6.

### **2.3.1 Image Acquisition and Segmentation**

Images for radiomics analysis can be acquired through various modern imaging techniques including CT, MRI, and PET. Numerical data can be extracted from these images, however, there must be a standardized image reconstruction protocol to remove variations in the intrinsic image properties that are not due to biological effects; an alternative method would be to introduce error bars to take these measures into account. Identifying the volume of interest through image segmentation is fundamental in radiation oncology. The identified volume is called the region of interest (ROI). There may be one or more tumor sites detected from one image and it is important to identify all suspected lesions as the volume of interest. This step is crucial since all subsequent processes depend on the segmented volume. Currently, images can be segmented manually by radiologists or by automated computer-aided segmentation. The general consensus is that automated segmentation yields higher reproducibility due to the individual variability in manual segmentation.

### **2.3.2 Radiomic Features Extraction**

Radiomic features extraction from the segmented images is the essence of this pipeline. The features can be separated into two broad categories which are semantic and agnostic. A subset of features in each category are shown in Table 2.1. Semantic features are used to describe the regions of interest by visual assessment of radiologists. Agnostic features on the other hand quantitatively capture tumor characteristics based on mathematical and statistical analysis. The latter can be further divided into four classes described below:

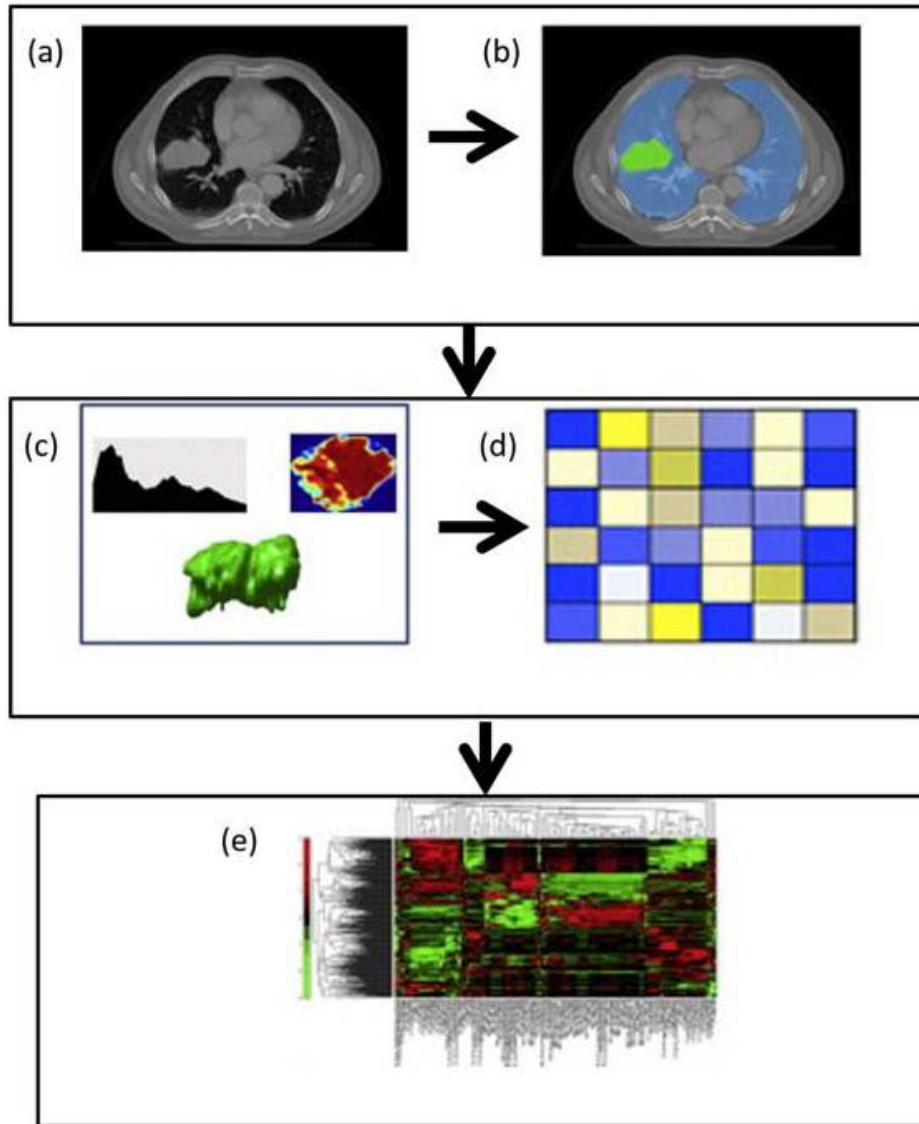


**Figure 2.6: Radiomics analysis pipeline.** (a) Image acquisition via computed tomography. (b) Image segmentation is performed on the lesion to identify the ROI. (c) Radiomic features are extracted from the ROI. The three feature categories are gray level patterns, inter-voxel relationships, and shape. (d) Analysis and classification of a subset of selected features. (e) Selected features are used as biomarkers in diagnosis and patient prognosis. Figure from [30]

- *morphological features* are used to define the shape of the defined ROI. Size, shape, sphericity, and compactness are a subset of features that fall under this category. For instance, compactness of a 2D segmented image can be computed using the perimeter to surface ratio of the ROI, given by

$$\text{perimeter to surface ratio} = \frac{P}{A},$$

where P is the perimeter and A is the area of ROI. A smaller ratio indicates a more compact (circular) shape.

- *First-order statistical features* describe the individual voxel without considering the spatial relationship to the surroundings. A subset of first-order features includes histogram-based relationships that are summarized into single values such as mean, maximum, minimum, asymmetry, and flatness. For example, the mean pSUV value of the region of interest can be calculated by the following equation:

$$\text{mean} = \frac{1}{N_p} \sum_{i=1}^{N_p} \mathbf{X}(i),$$

where  $N_p$  is the number of voxels in the ROI and X is the set of pSUV values of the individual voxels in the ROI.

- *Second-order texture features* characterize the texture of the ROI, or the spatial and statistical relationships between pixels. Texture analysis was first introduced by Haralick in 1973, which significantly enhanced the study of intratumoral texture heterogeneity [16]. Gray level co-occurrence matrices (GLCMs) was introduced by Haralick as one of the earliest methods for texture features extraction. This matrix (P) is an (N x N) square matrix with N possible number of gray levels from an image. The (i,j)th entry of P tells us the number of times a pixel with intensity i is adjacent to that of j. Note that adjacency is defined in four directions (right-horizontal, up-vertical, left and right upper diagonal) as shown in Figure 2.7 (a). Several matrices can be computed using different combinations of the distance (D) and angle ( $\theta$ ) parameters. An example of how the GLCM matrix is computed is shown

in Figure 2.7 (b), and the entries indicate how often a specific offset value occur between pixel pairs in the image.

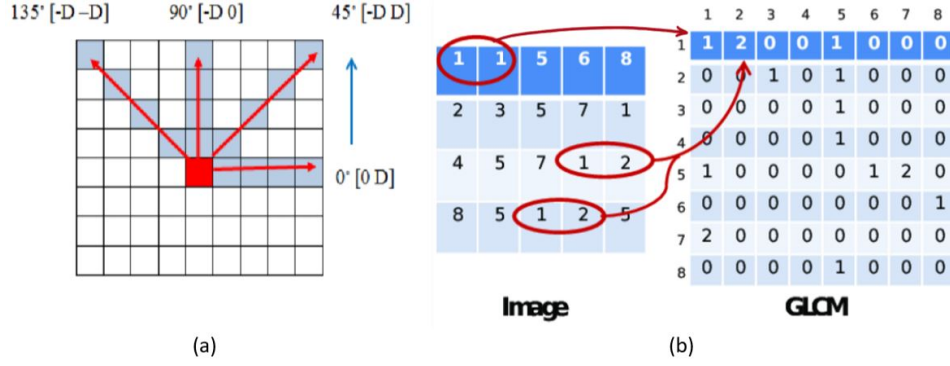


**Figure 2.7: Gray level co-occurrence matrix computation.** (a) Shows how adjacency is defined given a pixel of interest (red). The four possible angles are labeled and any choice of distance can be used to compute the GLCM. (b) An example of how an image matrix is translated to a GLCM matrix. The parameters used are  $D=1$  and  $\theta = 0^\circ$ . Figure adapted from [25] and [4].

Contrast is one of the Haralick features:

$$contrast = \sum_{i=1}^{N_g} \sum_{j=1}^{N_g} (i - j)^2 p(i, j).$$

The term  $p(i, j)$  refers to the normalized co-occurrence matrix given by

$$\frac{\mathbf{P}(i, j)}{\sum \mathbf{P}(i, j)}.$$

In general terms, contrast indicates variations in local intensity, where high contrast correlates to greater differences in intensity.

Homogeneity is another example of an Haralick feature:

$$homogeneity = \sum_{i=1}^{N_g} \sum_{j=1}^{N_g} \frac{p(i, j)}{1 + |i - j|}.$$

This value measures local homogeneity and a larger value indicates more

**Table 2.1:** Semantic and agnostic radiomic features

Semantic features	Agnostic features (Quantitative))
Size	Skewness (asymmetry)
Shape	Haralick textures
Location	Wavelets
Vascularity	Laws textures
Necrosis	Fractal dimensions

uniformity.

- *Higher-order statistical features* elicit repetitive and non-repetitive patterns imposed on images with filter grids. Filter transform of images refers to multiplying an image by a specific filter matrix. For instance, wavelet transform filters multiply the image by a matrix of complex waves to decompose the image into details, and Laplacian transform filters extract coarse texture patterns from the images.

### 2.3.3 Features Analysis

The main approach for radiomic feature analysis is through machine learning algorithms. The program learns from a given data set and becomes capable of identifying patterns with minimal human intervention when new sets of data are given. The automation of large quantity segmentation and extraction of image features enabled a fast and efficient data-driven analysis of medical images. Over 1000 radiomic features have been identified from numerous ROIs; however, the reproducibility and significance of each feature have been achieved in only a small subset of the features. Such a large complex data set may lead to over-fitting of the data; thus, identifying select features that are robust to noise and produce quality data is an important step in radiomic analysis. Identification of ideal radiomic features enables important diagnostic, prognostic, and predictive information to be captured from the images. Many suggest that will eventually become routine practice in clinics for a more precise diagnosis and patient-specific decision-making [15].

## 2.4 Hybrid Mathematical Modeling

The tumor growth simulation model uses mathematical oncology which is a method to study cancer using mathematics and simulation. The hybrid part of this model is the use of both agent-based models and partial differential equation models (PDEs) to simulate realistic tumor microenvironments. PDEs store information, such as concentration on each grid location, and use mathematical relationships to track the changes in values due to diffusion and consumption of molecules. Agents, namely autonomous decision-making entities, have access to the information from the PDEs which is used to determine the current state and the following action in each iteration step. The two components are completely decoupled and are executed independently while allowing the exchange of information between the grids. This allows any combination of agent grids and PDE grids for a flexible hybrid modeling (Figure 2.8). The particular strength of the hybrid model is that it provides insights into mechanistic feedback between the tumor cells and tumor tissue environment.

### 2.4.1 Agent Grid

The agent grid in this simulation is used as a container for the agents, in this case, the different types of tumor cells. The specific grid used is a 2D on-lattice grid where the agents are bound to lattice locations rather than a continuous plane. The agent occupies a pixel in the grid space and keeps track of its location as well as its current state. The agents can sample the neighbouring locations to determine the local population and decide if it can proceed with cell division.

### 2.4.2 Partial Differential Equation Grid

Tumor tissue is dynamic and the tumor local microenvironments are constantly changing. In our tumor growth model, we use 2D continuous partial differential equations to simulate the concentration of various molecules in the biological system. The PDE grids can model the complex internal dynamics while updating the concentration fields in each grid location to mimic realistic tumor tissue microenvironments at a microscopic level. The dynamics include diffusion of nutrients and consumption by cells on the agent-based model. Diffusion is run by adding deltas

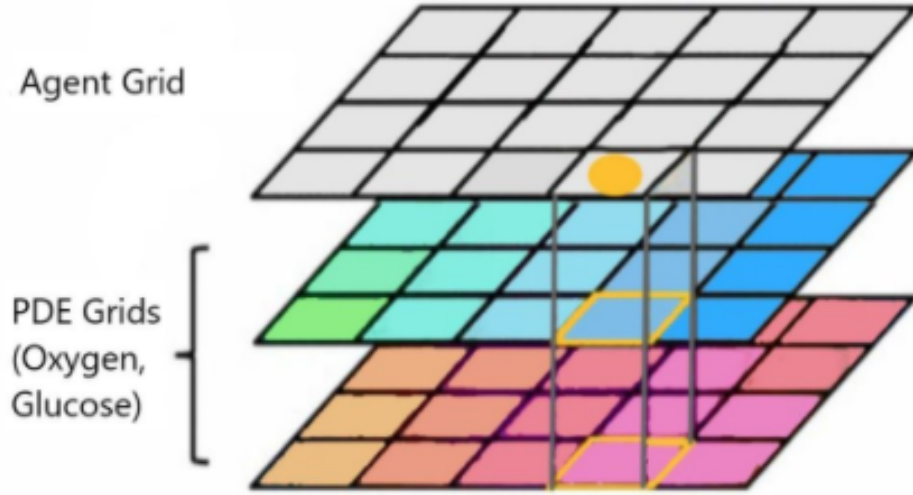


**Figure 2.8: Hybrid mathematical modelling with agent and PDE grids.**

The illustration shows one agent grid holding an agent (yellow dot) and two PDEs for oxygen and glucose. All grids can interface easily and the agent can retrieve the information from the corresponding pixels in the PDEs (yellow border).

to the current field with a wrap-around (periodic) boundary condition. This means that the simulation grid is surrounded by identical translated copies of itself. Periodic boundary conditions are often used to simulate a small part of a larger tissue to minimize edge effects.

The consumption of molecules follows the Michaelis-Menten (MM) kinetics since the consumption of molecules depends on the enzymatic turnover rate to harvest ATP. The chemical formula for this reaction is



where E stands for an enzyme, S for substrate, and ES for the enzyme-substrate complex. The consumption rate equation is given by

$$f = -V_{max} * \frac{[S]}{K_M + [S]},$$

where  $f$  is the rate of reaction,  $V_{max}$  is the maximum rate of the system, and  $K_M$  is the concentration of substrate at half the maximum rate. Glucose consumption is dependent on the ATP needs of the cell. Tumor cells have a greater energy demand to maintain their uncontrolled growth, requiring a larger  $V_{max}$ . Thus, the tumor cells in the model have  $V_{max}$  which is 10-20 times higher compared to normal cells.

An assumption was made in the model that the oxygen consumption rate for each cell type is constant. This is because  $K_M$  for oxygen in tissue is significantly lower than the oxygen concentration in tissue ( $K_M \ll S$ ), simplifying the model to

$$f = -V_{max} * \frac{[S]}{K_M + [S]} = -V_{max}.$$

The diffusion of molecules was modeled by Fick's diffusion law, together with the consumption of molecules. The equation is given by

$$\frac{\partial C}{\partial t} = D\nabla^2 C + f_i$$

The parameters are concentration ( $C$ ), time ( $t$ ), diffusion coefficient ( $D$ ), and consumption rate of molecules ( $f_i$ ).

Finally, knowing the consumption rates of oxygen and glucose, we can calculate the ATP production rate which will be used to partially determine the necrosis behavior of the cells in this model. The total aerobic respiration yields  $\sim 27$  ATP per glucose molecule as seen in section 2.1.1. Cancer cells that shift their metabolic pathway to glycolysis produce  $\sim 2$  ATP per glucose molecule. Thus the overall ATP production rate is given by

$$f_{ATP} = -(2f_G + \frac{27f_O}{5}).$$



## Chapter 3

# Methods

### 3.1 Tumor Growth Model

We model realistic tumor growth in vascularized tissue to study the relationship between measurable PET radiomic features and distinct tumor phenotypes. The simulation consists of one agent grid and two partial differential equation grids. The agent grid holds the different cell types and cross-sectional capillaries. The PDE grids have two main roles: tracking the concentration of nutrients at each grid location, and adding differentials (diffusion and consumption) of the molecules until a steady state is reached. The two PDE grids in the model track the oxygen and glucose concentrations at each pixel. The full list of realistic biological parameters used in this model can be found in Table 3.1. All three grids in the model are executed independently while the agents have access to the PDE grid data at all times. This is especially important since the type of the agent and its behavior depends on the concentration of nutrients, just like real cells in a biological system. The simulated grid size was 1000x1000 cells (2x2cm).

#### 3.1.1 Types of Agents

The four types of agents in the model are normal tumor, hypoxic tumor, necrotic tumor cells, and capillaries. The agent type is determined by the local concentration of nutrients that can be tracked using the PDE grids. Due to the altered cellular metabolism in cancer cells, each type of agent has its unique consumption rates for

**Table 3.1:** Model biological parameters

Biological constant	Values
Average cell (unit) size [ $\mu m$ ]	20
Average time for aerobic cell division [hours]	24
Capillary density range [ $\#/mm^2$ ]	20-100
Oxygen diffusion coefficient in tissue [ $cm^2/s$ ]	$1.65 \times 10^{-5}$
Glucose diffusion coefficient in tissue [ $cm^2/s$ ]	$2.7 \times 10^{-6}$
Oxygen flux from capillary [mol/min/unit]	$2.81 \times 10^{-12}$
Glucose concentration in capillary [mol/L]	$5 \times 10^{-3}$
Oxygen consumption rate - normal tumor [mol/min/cell]	$4 \times 10^{-15}$
Oxygen consumption rate - hypoxic tumor [mol/min/cell]	$2 \times 10^{-15}$
Oxygen consumption rate - non-cancer cell [mol/min/cell]	$2.5 \times 10^{-18}$
Glucose $V_{max}$ - normal tumor [mol/min/cell]	$5 \times 10^{-14}$
Glucose $V_{max}$ - hypoxic tumor [mol/min/cell]	$1.02 \times 10^{-13}$
Glucose $V_{max}$ - non-cancer cell [mol/min/cell]	$5 \times 10^{-15}$
Glucose $K_M$ [mol/min/cell]	$2 \times 10^{-14}$
Death ATP production rate (DPR) [mol/min/cell]	$2.57 \times 10^{-14}$

nutrients; the oxygen consumption rate is constant for each cell type, whereas the glucose consumption rate depends on the local concentration of glucose. Capillaries were modeled as cross-sectional points and initialized with uniform density or completely randomized placements across the agent grid. In between each diffusion step, the nutrient concentrations in the capillaries were reset to the basal levels in the blood, as the source of glucose and oxygen that diffuse through the tissue.

### 3.1.2 Simulation Details

Agents are able to determine its current state and the behaviour in the following round of iteration by accessing the information on the PDE grid that tracks the oxygen and glucose concentrations. The decision-making process of an agent is shown as a flowchart in Figure 3.1. First, the simulation model is initialized by placing blood vessels and diffusing them until a steady state. Once a steady state is reached, a single normal tumor cell is implanted at the center of the grid. This cell goes through a series of conditional questions where the cell determines whether it will remain a normal tumor cell, or turn into a hypoxic or necrotic cell. The

cell turns hypoxic when the oxygen concentration at that cell location is below a threshold level (values listed in Table 3.1). Cell necrosis happens when the ATP production rate falls below the death rate or if the oxygen level is below the death concentration. This state determination mechanism is based on the realistic behaviour of a cancer cell *in vivo* as explained in section 2.1.

Agents can also divide to produce a daughter cell of the same type. Only normal tumor cells and hypoxic cells can go through division and the probability depends on the concentration of oxygen and glucose to generate ATP. When the cell meets the condition to divide, it samples the surrounding Moore neighbourhood (Figure 3.2) to look for an available location. Available locations are non-cancer cell or vessel locations.

The parameters that were adjusted to simulate various tumor phenotypes were 1) blood vessel density, 2) spatial arrangement of vessels (random or uniform density), 3) probability of vessel removal, and 4) probability of death by insufficient nutrients. The probability of vessel removal by a tumor cell was used to simulate the extent of vessel obstruction in real solid tumors. The death probability was implemented because the cells do not die immediately after depletion of nutrients; instead, prolonged shortage of oxygen or glucose is required for necrosis. For all simulations, the death probability due to shortage of oxygen was

$$P = 1 - \frac{\text{local concentration}}{\text{necrotic concentration}},$$

and that of ATP was either the same as oxygen or

$$P = 1 - \left( \frac{\text{local concentration}}{\text{necrotic concentration}} \right)^2.$$

## 3.2 Translating Simulated Images to PET Images

The tumor growth simulation state is exported every 10 hours of biological time in the TIFF file format. The time-sequenced simulated images are then translated into synthetic PET images for further analysis using radiomics. The translation step involves two key steps: mapping the agent locations and associating them with radiotracer uptake values, and matching the resolution of the simulated images

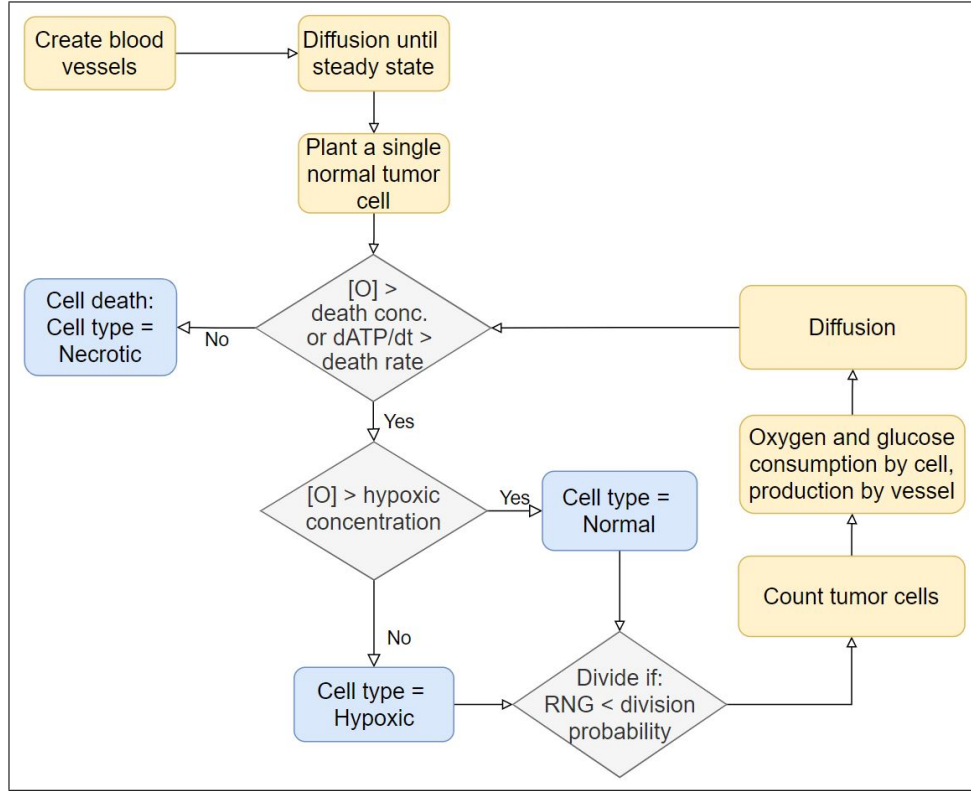


**Figure 3.1: Tumor growth simulation flowchart.** The flowchart shows the step sequence of how the simulation is initialized, how agents determine their state, and how the PDE grids function (diffusion and consumption of molecules)

to PET images. The time sequences of simulated cell maps were converted into pseudo standardized tracer uptake value (pSUV) for the  $^{18}\text{F}$ -FDG tracer, which is dependent on the type of individual cells. The relative tracer uptake values were 1, 8, 12, 0 for normal cells, tumor cells, hypoxic tumor cells, and necrotic cells, respectively. Next, we used a Gaussian filter with a smoothing kernel to reduce the simulated image resolution of  $20\mu\text{m}$  to a typical PET resolution of  $\sim 3\text{mm}$ . Lastly, realistic intensity Gaussian noise was also added to make it more clinically relevant. An example of time-sequenced translated images are shown in Figure 4.2.

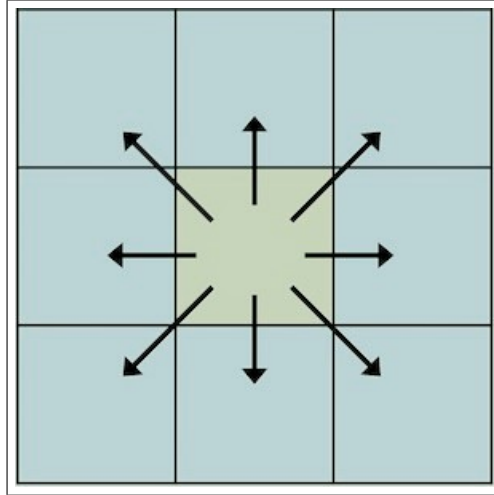


**Figure 3.2: Moore neighbourhood.** Represents the eight locations surrounding the center pixel, in this case an agent, that border an edge or a corner of the cell. The arrows indicate the possible locations an agent can divide into in a Moore neighbourhood. Figure adapted from [9]

### 3.2.1 Advantages of Using Synthetic PET Images

There are two clear reasons to why we chose to use synthetic PET images from the tumor growth simulation for radiomics analysis. First, the model begins from a single tumor cell allowing us to obtain images throughout the progression of tumor growth to study the evolution of image features with biological time. Such information is impossible to obtain from human subjects since PET imaging involves ionizing radiation that limits the maximum radiation dose that can be administered to a patient. The second advantage is that we can test with any combination of biological parameters in the simulation within the biologically feasible range to study the affects on tumor progressions and image properties. The hybrid model is also extremely flexible and allows us to add layers of PDE grids to model with different molecules of interest.

### 3.3 Radiomics Analysis

The translated synthetic PET images were analyzed using MATLAB functions for radiomics analysis which is used widely in radiomics research. We used the typical 40%  $SUV_{max}$  to determine the ROI in the synthetic PET images. To assess the plausibility of our model, we computed four conventional PET radiomic features that have been validated for its reproducibility and significance [22]. The four features are mean pSUV, shape-compactness, texture-contrast, and texture-homogeneity. The simulations produced time sequenced images of tumor growth at every 10 biological hours, so the features were also extracted at the same interval. For the extraction process, all ROI's were converted into gray-scale to generate gray-level co-occurrence matrices with all four offsets defined as described by Haralick. The list of MATLAB functions and user-defined functions used for the analysis is shown in Table 3.2.

<b>MATLAB Function</b>	<b>Description</b>
graycomatrix(I, P)	Creates a gray-level co-occurrence matrix (glcm) from image I and other parameters P, such as offsets and number of gray levels.
graycoprops(glcm)	Outputs several statistical properties from the glcm. Properties include Contrast, Correlation, Energy, and Homogeneity.
sphericityValue	Outputs compactness of the ROI by calculating the perimeter to surface area ratio.
meanData	Computes the mean pSUV value of the ROI by averaging the values of all pixels.

**Table 3.2:** MATLAB functions for radiomics analysis.

## Chapter 4

# Results

### 4.1 Agent Grid + Oxygen PDE Grid

We were able to generate three types of tumors with distinct phenotypes using different combinations of microparameters in the hybrid mathematical model for tumor growth (Figure 4.1). The adjusted parameters were blood vessel density (Types A,C:  $20/mm^2$ , Type B:  $100/mm^2$ ), spatial arrangement of vessels (A,C: Random placement, B: Uniform density placement), and tumor vascular network alterations. The third parameter specifically refers to the obstruction of blood vessels due to tumor growth; this was modelled by introducing a probability of vessel removal (A,B: 1, C: 0,05) by a cancer cell when the cell attempts to divide into a vessel location. The vessels that are first to be obstructed represent smaller vessels and the ones that remain until later stages of tumor growth depict larger vessels in solid tumors.

The resulting simulated tumor images were translated into synthetic PET images with each pixel reflecting the corresponding pSUV values. Figure 4.2 shows a series of translated Type C tumor images with its longitudinal growth. This demonstrates that we can study the progression of the PET images properties with tumor growth, which is one of the advantages of using the simulation as discussed in the previous sections.

The synthetic PET images of the three different types of tumor were visually distinguishable in the corresponding mean pseudo standard uptake value (pSUV)

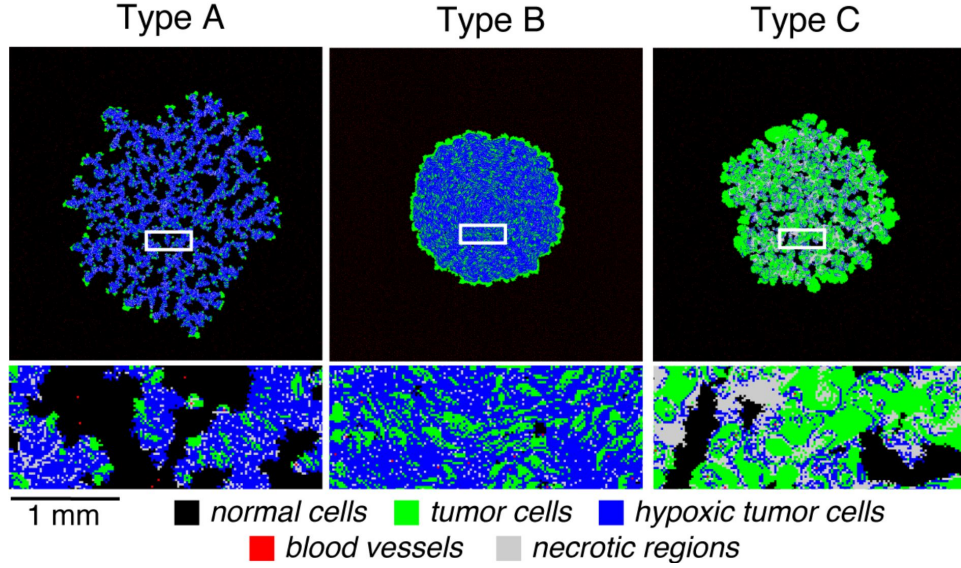


**Figure 4.1: Simulated tumors with distinct tumor phenotypes.** The model with different combinations of tumor tissue microenvironments was able to produce three tumor types with distinct tumor phenotypes.

PET images, reflecting the distinct phenotypic profiles. The comparison of the growth rates for each type demonstrated that the model was able to produce diverse and realistic growth rates of about 80-310 days to grow a 1cm diameter tumor (Figure 4.3). Using MATLAB radiomics analysis library, four radiomic features were computed from the generated images: mean pSUV, shape-compactness, Haralick texture-contrast, and Haralick texture-homogeneity. As shown in Figure 4.4, these radiomic feature values were plotted as a function of tumor progression in biological hours. Numerical values of the four features at their fully grown size are listed in Table 4.1. With distinguishable feature values between tumor types, the combination of the four features enables unique association of the tumor phenotype with its specific tissue parameters.

## 4.2 Agent Grid + Oxygen and Glucose PDE Grids

Followed by the simulation with the oxygen PDE grid, the model was further developed by adding a glucose PDE grid to track the ATP production rate based



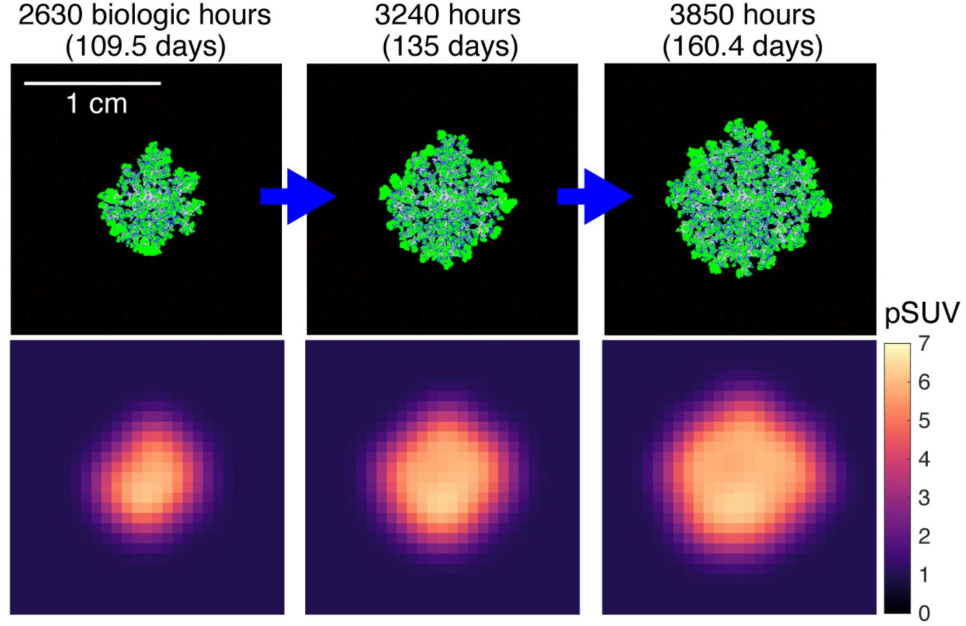


**Figure 4.2: Translation of the Type C tumor longitudinal growth simulation to PET images.** Simulated images were translated into synthetic PET images by converting the cell map into corresponding pSUV values.

**Table 4.1:** Radiomic feature values for 1cm tumors.

Feature	Type A	Type B	Type C
pSUV	$4.58 \pm 0.03$	$7.63 \pm 0.72$	$4.71 \pm 0.04$
Compactness	$0.91 \pm 0.01$	$0.95 \pm 0.01$	$0.94 \pm 0.005$
Contrast	$1.67 \pm 0.08$	$1.58 \pm 0.04$	$1.36 \pm 0.1$
Homogeneity	$0.71 \pm 0.01$	$0.80 \pm 0.006$	$0.79 \pm 0.01$

on the nutrient concentrations. By changing the death probability from ATP deficiency (Type D:  $1 - \frac{[ATP]_{local}}{DPR}$ , Type E:  $1 - (\frac{[ATP]_{local}}{DPR})^2$ ), vessel density (D:  $20/mm^2$ , E:  $100/mm^2$ ), and vessel removal probability (D: 0.05, E: 1), we were able to generate two tumors with distinct phenotypic profiles. The preliminary results from this simulation model are shown in Figure 4.5. Tumor type D showed significantly increased tumor tissue dynamics throughout its growth compared to tumor type C, which was simulated with the same blood vessel density and vessel removal prob-

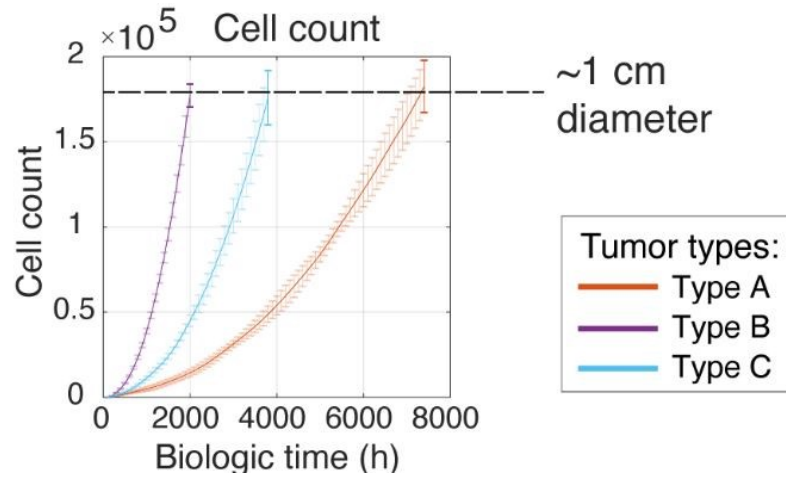


**Figure 4.3: Biological time for tumor growth.** The cell count was plotted against the biological time to compare the growth rate of each tumor type. The tumors were grown up to  $\sim 1\text{cm}$  in diameter.

ability. The images also portray more realistic tumor tissue characteristics, which closely resemble a molecular or histological image of a tumor. By simulating tumor Type E, we were able to demonstrate that a necrotic core can be modelled using this tumor growth simulation. With maximum vessel removal probability and increased death probability from ATP deficiency, a pronounced necrotic region was generated with viable cells surrounding only the grid locations in close proximity of active vessels.

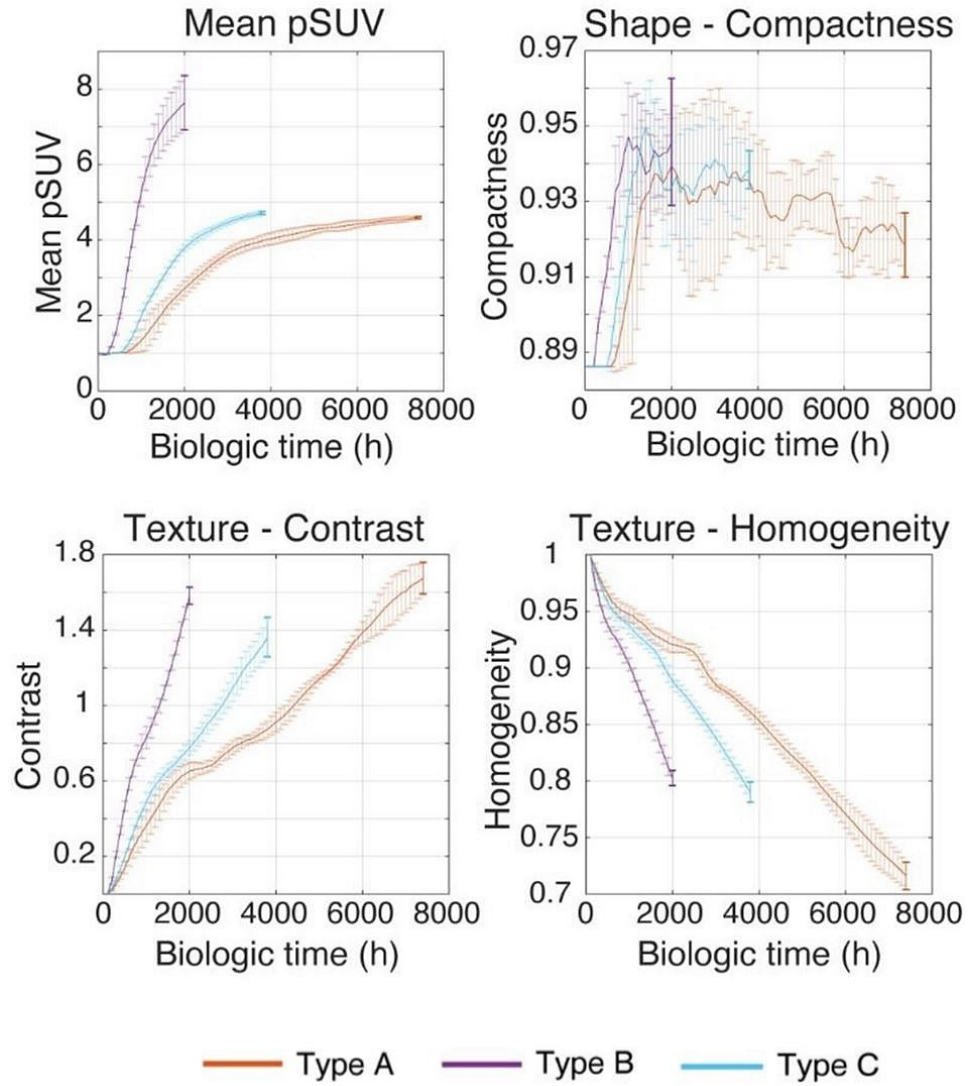


**Figure 4.4: Radiomics analysis on synthetic PET images.** Four PET radiomic features were plotted against simulated biological time for tumor growth. The mean and standard deviations of the data points were calculated using three separate tumor growth simulation rounds. The error bar represents one standard deviation.

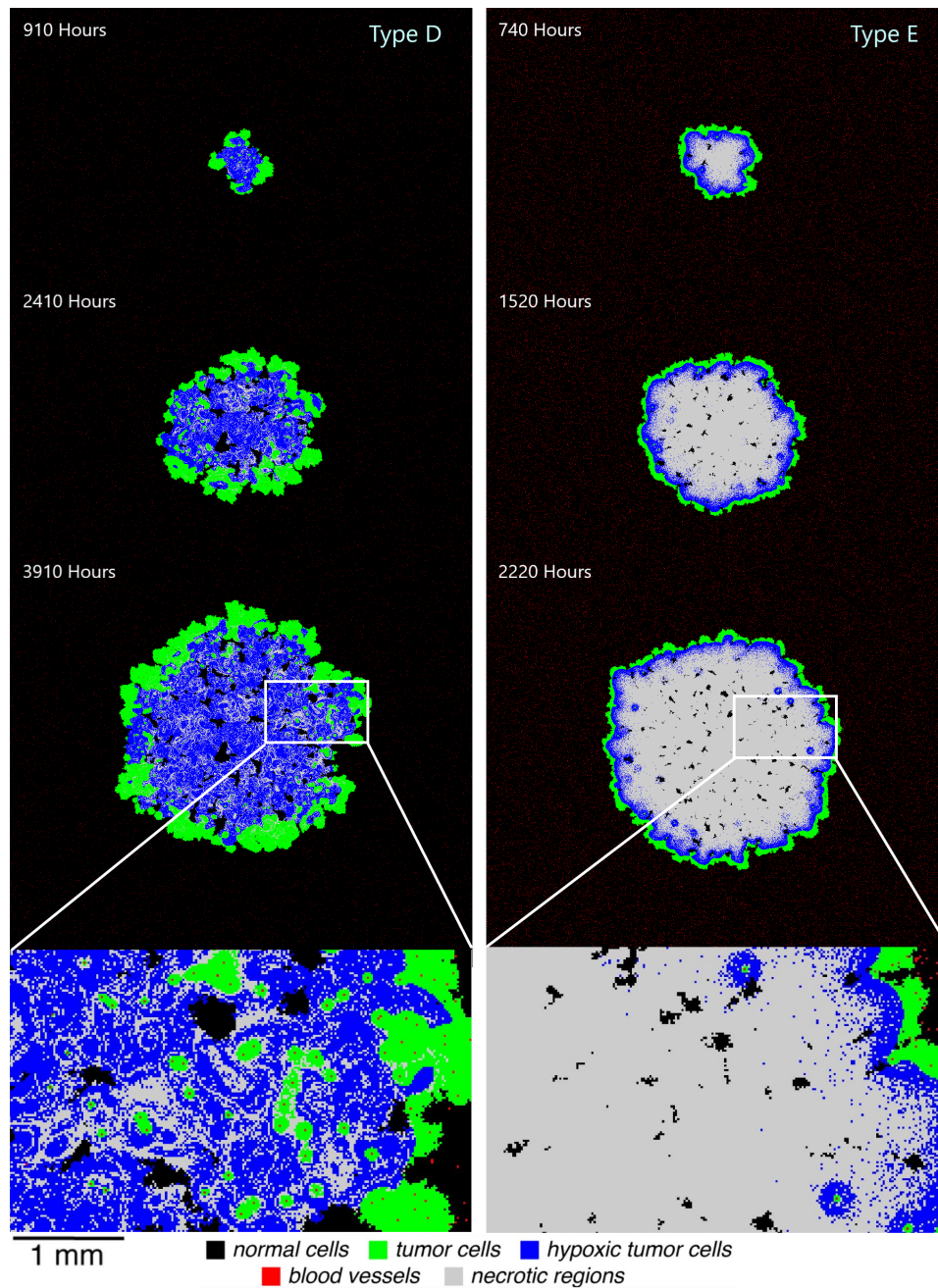


**Figure 4.5: Two distinct tumor phenotypes simulated with oxygen and glucose PDE grids.** The tumor progression is shown at three different time points (biological hours) until it reached 1cm in diameter. The bottom panels represent the magnifications of the regions indicated with the white box.

## Chapter 5

# Discussion

Tumor population is highly heterogeneous and under constant evolution towards more malignant phenotypes which challenges effective cancer diagnosis and treatment planning. Heterogeneous tumor cell populations have different sensitivity to treatment. However, molecular classification of tumors are difficult to achieve with the small region sampling due to intratumoral heterogeneity. In contrast, medical imaging allows for visualization of heterogeneity in the entire tumor region. This motivated us to develop the tumor growth model for studying the microscopic changes and characteristics of tumor tissues reflected in PET imaging. We were able to successfully generate five distinct tumor profiles using different combinations of biological parameters.

The first three tumor types simulated with the oxygen PDE grid (Types A-C) were analysed using quantitative PET radiomic features which showed distinct progression patterns with tumor growth. This suggests that realistic tumor growth can be achieved via simulating tumor tissue and its parameters, and the resulting microscopic tumor phenotypes are measurable through PET imaging. This allows us to establish the 1:1 correspondence between tumor phenotypic parameters and PET radiomic features, which can be used as image-based biomarkers for cancer diagnosis, prognosis, and tracking treatment outcomes.

The improved version of the simulation with the addition of glucose PDE was able to produce two visually distinguishable tumor phenotypes. The addition of glucose PDE grid significantly enhanced the ability to show the dynamics of the

tumor tissues throughout their development. The resulting images were also displaying more realistic features of solid tumors. In tumor Type D, the gradual removal of smaller vessels resulted in viable tissue surrounding the larger vessels that have not been removed; beyond the diffusion-limited range from the vessels was a mixture of hypoxia and necrosis with some accumulation of necrotic cells. The simulation of the Type E tumor features a definite necrotic core. With vessel removal probability of 1, simulating the vessel removal including the larger ones, we could observe that the center of the tumor became completely necrotic. These results are consistent with what was seen in real solid tumor progressions studied by other groups [11, 13, 38].

Medical imaging is known for its macroscopic visualization of tumor heterogeneity due to limited resolution of the imaging techniques. In this study, we demonstrated that microscopic changes in tumor tissue can be observed and tracked through macroscopic PET images via a novel method of using a tumor growth simulation model. This opens up the potential for radiomics studies on microscopic tumor properties that could replace or complement histopathological approaches to associate the predictive radiomic models with biological significance. Microscopic information from the radiomic analysis would reduce the needs of invasive sampling and molecular assays that are costly and burdening to patients. Additionally, the current methods of biopsies on a small region of tumor cannot fully capture the state due to the spatial and temporal heterogeneity. Contrarily, medical imaging is a much less invasive method that can capture the entire region of interest; it provides a wealth of information that can be used to monitor tumor progression and response to treatment. This also provides a significant potential to largely advance precision medicine that have been hindered by the limitation to fully capture spatial and temporal tumor heterogeneity through conventional sampling methods [2].

There are a few limitations to the simulation and its applications for back tracking the biological parameters from lower resolution PET images. Our method of down-sampling the simulated tumor images to PET image resolution to see how the microscopic changes are reflected in PET scans was a convenient process relative to the reverse process. However, backtracking from the macroscopic PET images to microscopic tumor properties would be much more difficult. This suggests that, the mechanism for extrapolating the biological parameters and tumor phenotypes

given a real PET image still remains a challenge. Also, the model has an upper limit to the dimensionless diffusion coefficient of molecules and any value over the limit will disturb the partial differential equations making it unstable. This requires time increment of the diffusion and consumption steps to be extremely small ( $\sim 0.03s$  in this model) relative to the cellular (agent) time step of 1 hour between every iteration. This required thousands of diffusion steps between cell steps to achieve steady state, which demands for a progressively greater computational power.

## Chapter 6

# Future Directions

This study demonstrated the possibility of using tumor growth simulations to study the relationship between tumor tissue microparameters and the resulting heterogeneous tumor phenotypic profiles captured in PET images. The identified 1:1 link between PET image features and tumor tissue characteristics can be used as image-based biomarkers for personalized cancer diagnosis and treatment planning.

The unique strength of the hybrid model allows for further expansion and development of the model with additional PDE grids. For instance, the altered metabolism increases acid production, which affects the pH of the microenvironments [6]. Tumor cells are better adapted to acidic conditions than normal cells which promotes their aggressive growth and invasion into normal tissue. Another example is polypeptide growth factors (GF) associated with cancer progression; these molecules are involved in resistance to therapy and colonization of distant tissues [37]. All of these could be incorporated into the hybrid model by adding PDE grids for protons ( $H^+$ ) and GF for a more realistic simulation. The increased biological relevance could offer more insight into the interlink between PET image properties and tumor tissue characteristics. Once the model becomes complete enough to accurately simulate a real biological tissue, it can be used as a reference for simulating the effectiveness of cancer drugs and radiation therapy.

Another improvement can be made in the translation process of simulated images into synthetic PET images. The current method was to translate the relative tracer uptake values of the cell types into pSUV values and to apply the Gaussian



filter and noise across the entire image. However, this does not account for the many sources of errors in a realistic PET scan, such as scatter and random coincident events. A more realistic approach for the translation would be to perform a Monte Carlo simulation of the photon emission (while the two emitted photons make a  $180^\circ$ ) with annihilation rates that depend on the individual cell's glucose consumption rates. Here, the consumption rates can be obtained and stored from the simulation as an image matrix at each cell step. The simulated photon emissions can be detected by a hypothetical detector ring and the sinogram produced can be reconstructed into a synthetic PET image.

Lastly, the current model simulates tumor growth in 2D (a plane of a single layer of cells) , while real solid tumors would grow in three dimensions. Tumor growth simulation in 3D can be done using the hybrid mathematical model with a 3D lattice grid. Adding the third dimension will certainly make the model more realistic and applicable to the biological systems.

# Bibliography

- [1] The personalized medicine report. opportunity, challenges, and the future, 2017. → pages 3
- [2] H. J. W. L. Aerts. The Potential of Radiomic-Based Phenotyping in Precision Medicine: A Review. *JAMA Oncology*, 2(12):1636–1642, 2016. doi:10.1001/jamaoncol.2016.2631. → pages 3, 36
- [3] W. Al Tameemi, T. P. Dale, R. M. Al-Jumaily, and N. R. Forsyth. Hypoxia-modified cancer cell metabolism. *Frontiers in Cell and Developmental Biology*, 7, 2019. doi:10.3389/fcell.2019.00004. → pages vi, 8, 9
- [4] M. Ashfaq, N. Minallah, Z. Ullah, A. M. Ahmad, A. Saeed, and A. Hafeez. Performance analysis of low-level and high-level intuitive features for melanoma detection. *Electronics*, 8(6), 2019. doi:10.3390/electronics8060672. → pages viii, 18
- [5] T. Beyer, D. Townsend, T. Brun, P. Kinahan, M. Charron, R. Roddy, J. Jerin, J. Young, L. Byars, and R. Nutt. A combined pet/ct scanner for clinical oncology. *Journal of Nuclear Medicine*, 40(8):1369–1379, 2000. → pages vi, 2
- [6] E. Boedtkjer and S. F. Pedersen. The acidic tumor microenvironment as a driver of cancer. *Annual Review of Physiology*, 82(1):103–126, 2020. doi:10.1146/annurev-physiol-021119-034627. → pages 38
- [7] F. Bray, J. Ferlay, I. Soerjomataram, R. L. Siegel, L. A. Torre, and A. Jemal. Global cancer statistics 2018: Globocan estimates of incidence and mortality worldwide for 36 cancers in 185 countries. *CA: A Cancer Journal for Clinicians*, 68(6):394–424, 2018. doi:10.3322/caac.21492. → pages 1
- [8] R. Chandra and A. Rahmim. Wolters Kluwer, 8 edition, 2017. ISBN 9781496381842. → pages 11

- [9] P. Compeau. Chapter 3: Discovering a self-replicating automaton with top-down programming. → pages viii, 27
- [10] G. M. Cooper and R. E. Hausman. *The Development and Causes of Cancer*. ASM Press, 2003. → pages 5
- [11] H. Eddy and G. Casarett. Development of the vascular system in the hamster malignant neurilemmoma. *Microvasc Res*, 6(1):63–82, 1973. doi:10.1016/0026-2862(73)90007-1. → pages 8, 36
- [12] S. Elmore. Apoptosis: A review of programmed cell death. *Toxicologic Pathology*, 35(4):495–516, 2007. doi:10.1080/01926230701320337. → pages 10
- [13] J. Forster, W. Harriss-Phillips, M. Douglass, and E. Bezak. A review of the development of tumor vasculature and its effects on the tumor microenvironment. *Hypoxia*, Volume 5:21–32, 2017. doi:10.2147/hp.s133231. → pages 36
- [14] P. E. Galavis, C. Hollensen, N. Jallow, B. Paliwal, and R. Jeraj. Variability of textural features in fdg pet images due to different acquisition modes and reconstruction parameters. *Acta Oncologica*, 49(7):1012–1016, 2010. doi:10.3109/0284186x.2010.498437. → pages 4, 6
- [15] R. J. Gillies, P. E. Kinahan, and H. Hricak. Radiomics: Images are more than pictures, they are data. *Radiology*, 278(2):563–577, 2016. doi:10.1148/radiol.2015151169. → pages 3, 19
- [16] R. M. Haralick, K. Shanmugam, and I. Dinstein. Textural features for image classification. *IEEE Transactions on Systems, Man, and Cybernetics*, SMC-3(6):610–621, 1973. doi:10.1109/TSMC.1973.4309314. → pages 17
- [17] M. Hatt, M. Majdoub, M. Vallieres, F. Tixier, C. C. Le Rest, D. Groheux, E. Hindie, A. Martineau, O. Pradier, R. Hustinx, and et al. 18f-fdg pet uptake characterization through texture analysis: Investigating the complementary nature of heterogeneity and functional tumor volume in a multi-cancer site patient cohort. *Journal of Nuclear Medicine*, 56(1):38–44, 2014. doi:10.2967/jnumed.114.144055. → pages 4, 6
- [18] E. Hirata and E. Sahai. Tumor microenvironment and differential responses to therapy. *Cold Spring Harbor Perspectives in Medicine*, 7(7), 2017. doi:10.1101/cshperspect.a026781. → pages 3, 6

- [19] A. Ibrahim, S. Primakov, M. Beuque, H. Woodruff, I. Halilaj, G. Wu, T. Refaee, R. Granzier, Y. Widaatalla, R. Hustinx, and et al. Radiomics for precision medicine: Current challenges, future prospects, and the proposal of a new framework. *Methods*, 188:20–29, 2021. doi:10.1016/j.ymeth.2020.05.022. → pages vi, 4
- [20] P. Jacquet and A. Stéphanou. Why the tumor cell metabolism is not that abnormal. 2019. doi:10.1101/865048. → pages 7
- [21] V. Kapoor, B. M. McCook, and F. S. Torok. An introduction to pet-ct imaging. *RadioGraphics*, 24(2):523–543, 2004. doi:10.1148/rg.242025724. PMID: 15026598. → pages 13
- [22] M. M. Krarup, L. Nygård, I. R. Vogelius, F. L. Andersen, G. Cook, V. Goh, and B. M. Fischer. Heterogeneity in tumours: Validating the use of radiomic features on 18f-fdg pet/ct scans of lung cancer patients as a prognostic tool. *Radiotherapy and Oncology*, 144:72–78, 2020. doi:10.1016/j.radonc.2019.10.012. → pages 28
- [23] P. Krzyszczyk, A. Acevedo, E. Davidoff, L. Timmins, I. Marrero-Berrios, M. Patel, C. White, C. Lowe, J. Sherba, C. Hartmanshenn, K. O’Neill, M. Balter, Z. Fritz, I. Androulakis, R. Schloss, and M. Yarmush. The growing role of precision and personalized medicine for cancer treatment. *Technology (Singap World Sci)*, 6(3-4):79–100, 2018. doi:10.1142/S2339547818300020. → pages 3
- [24] M. V. Liberti and J. W. Locasale. Correction to: ‘the warburg effect: How does it benefit cancer cells?’. *Trends in Biochemical Sciences*, 41(3):287, 2016. doi:10.1016/j.tibs.2016.01.004. → pages 7
- [25] F. Mahmood and W. Abbas. Texture features analysis using gray level co-occurrence matrix for abnormality detection in chest ct images. *Iraqi Journal of Science*, 57:279–288, 02 2016. → pages viii, 18
- [26] B. McGuire and T. Secomb. Estimation of capillary density in human skeletal muscle based on maximal oxygen consumption rates. *Am J Physiol Heart Circ Physiol*, 285(6):2382–2391, 2003. doi:10.1152/ajpheart.00559.2003. → pages 8
- [27] A. Minchinton. Ubc phys 405: Radiation biophysics [powerpoint slides], 2020. → pages vi, 9, 10

- [28] F. Orlhac, M. Soussan, J.-A. Maisonobe, C. A. Garcia, B. Vanderlinden, and I. Buvat. Tumor texture analysis in 18f-fdg pet: Relationships between texture parameters, histogram indices, standardized uptake values, metabolic volumes, and total lesion glycolysis. *Journal of Nuclear Medicine*, 55(3): 414–422, 2014. doi:10.2967/jnumed.113.129858. → pages 4, 6
- [29] A. C. Papanicolaou. *Positron Emission Tomography: Blood Flow and Metabolic Imaging*. Oxford University Press, 2017. → pages vii, 11, 12, 14
- [30] V. Parekh and M. Jacobs. Radiomics: a new application from established techniques. *Expert Rev Precis Med Drug Dev*, 1(2):207–226, 2016. doi:10.1080/23808993.2016.1164013. → pages vii, 16
- [31] M. Robertson-Tessi, R. J. Gillies, R. A. Gatenby, and A. R. Anderson. The importance of metabolic heterogeneity and its consequences on tumor invasion, metastatic growth, and treatment. *Tumor Microenvironment*, 2013. doi:10.1158/1538-7445.tim2013-a2. → pages 8
- [32] S. Rockwell, I. Dobrucki, E. Kim, S. Marrison, and V. Vu. Hypoxia and radiation therapy: Past history, ongoing research, and future promise. *Current Molecular Medicine*, 9(4):442–458, 2009. doi:10.2174/156652409788167087. → pages 9
- [33] A. Tellechea, A. Kafanas, E. Leal, F. Tecilazich, S. Kuchibhotla, M. Auster, I. Kontoes, J. Paolino, E. Carvalho, L. Pradhan, and A. Veves. Increased skin inflammation and blood vessel density in human and experimental diabetes. *The international journal of lower extremity wounds*, 12, 02 2013. doi:10.1177/1534734612474303. → pages 8
- [34] Y. Tsujimoto. Apoptosis and necrosis: Intracellular atp level as a determinant for cell death modes. *Cell Death amp; Differentiation*, 4(6): 429–434, 1997. doi:10.1038/sj.cdd.4400262. → pages 10
- [35] T. C. Vander Heiden MG, Cantley LC. Understanding the warburg effect: The metabolic requirements of cell proliferation. *Science*, 324(5930): 1029–1033, 2009. doi:10.1126/science.1160809. → pages vi, 7
- [36] M. WIEDEMAN. Dimensions of blood vessels from distributing artery to collecting vein. *Circulation Research*, 12(4):375–378, 1963. doi:10.1161/01.RES.12.4.375. → pages 6
- [37] E. Witsch, M. Sela, and Y. Yarden. Roles for growth factors in cancer progression. *Physiology*, 25(2):85–101, 2010. doi:10.1152/physiol.00045.2009. → pages 38

- [38] H. Yamaura and H. Sato. Quantitative studies on the developing vascular system of rat hepatoma. *J Natl Cancer Inst*, 53(5):1229–1240, 1974. → pages 8, 36
- [39] J. Yokota. Tumor progression and metastasis . *Carcinogenesis*, 21(3): 497–503, 2000. doi:10.1093/carcin/21.3.497. → pages 5